Atmospheric Research 329 (2026) 108531

Contents lists available at ScienceDirect

Atmospheric Research

journal homepage: www.elsevier.com/locate/atmosres

Vertical evolution of precipitation and associated atmospheric parameters at Ny-Ålesund (78°55′N, 11°56′E) in the Arctic

Lekhraj Saini [a], Saurabh Das [a,*], Nuncio Murukesh [b]

[a] Department of Astronomy, Astrophysics and Space Engineering, Indian Institute of Technology Indore, Simrol, Indore, 453552, Madhya Pradesh, India
[b] National Centre for Polar and Ocean Research (NCPOR), Headland Sada, 403804, Goa, India

ARTICLE INFO

Keywords:
Vertical profile
Arctic precipitation
Snowfall
Micro Rain Radar

ABSTRACT

The Arctic is experiencing warming nearly twice the global average rate. This significantly affects its precipitation with the snow to rain and mixed phase transitions. Accurate characterization of these changes requires high-resolution vertical profiling of microphysical processes. This study combines surface observation with vertical profiles of the atmospheric parameters and precipitation to investigate the vertical evolution of different forms of Arctic precipitation. Data were collected from the Himadri Research Station, Ny-Ålesund (78°55′N, 11°56′E) in Svalbard, which is a key location along the atmospheric moisture transport pathway into the Arctic. Micro Rain Radar (MRR), disdrometer and ceilometer were used to characterize the type of precipitation and their microphysical evolution up to 6 km in altitude, along with the associated cloud base height. The study also explores seasonal variability in the vertical distribution of both liquid and solid precipitation and links their relationship with atmospheric parameters. Different types of precipitation show a varied behavior in terms of vertical evolution and were found to be highly sensitive within 1.5–2 km above the surface altitude. The results are expected to advance the understanding of Arctic precipitation processes, provide critical insights for improving satellite-based precipitation retrievals, and improve the performance of numerical weather prediction and climate models in polar regions.

1. Introduction

During the past century, the Arctic has experienced a warming rate nearly twice the global average, indicating the strong signature of climate changes (Ernakovich et al., 2014; Solomon et al., 2007; Hassol, 2004). Due to this high sensitivity to climate change in the Arctic region, there is a growing scientific interest in understanding the response of the Arctic hydrological cycle, given its potential to influence and amplify future climate variability through various feedback mechanisms (Schumacher and Houze Jr., 2006). Precipitation is an important part of the hydrological cycle, which is increasing in response to enhanced transport of subtropical moisture to the Arctic, as well as increased Arctic evaporation as potential mechanisms of modulation of the water cycle (Bintanja and Selten, 2014; Bengtsson et al., 2011; Kug et al., 2010). These changes also impact Arctic sea ice, glaciers, and fragile ecosystems as they are linked to the increase in greenhouse gases, leading to higher temperatures, ice melting, changes in storm patterns, changes in intensity and precipitation phase (Macdonald et al., 2005). The reduction in sea ice and the increase in Arctic precipitation are intricately linked. Arctic showing a substantially higher mean precipitation sensitivity (4.5%°C^{-1}) compared to the global average (1.6-1.9%°C^{-1}) (Bintanja and Selten, 2014).

Understanding Arctic precipitation has also become increasingly important due to projections of increased precipitation, particularly the liquid phase in the region (Bintanja and Selten, 2014; Bintanja et al., 2020; Walsh and Chapman, 1998; Maahn and Kollias, 2012). Positive trends in rainfall have been observed, particularly during winter (0.36 mm decade^{-1}) and autumn (0.79 mm decade^{-1}), which exceed the corresponding mean precipitation trends in winter (0.31 mm decade^{-1}) and autumn (0.36 mm decade^{-1}), respectively. These trends are associated with an increase in tropospheric moisture and temperature (Athulya et al., 2023).

The above concerns underscore the need to study the dynamics and microphysical processes that govern the formation and evolution of different hydrometeors in a changing environment. This requires accurate and detailed vertical observations of precipitation and associated atmospheric parameters in the vast, remote and often inaccessible Arctic region. Satellite observations are useful in monitoring such remote areas; however, there are certain limitations, such as coarse resolution and a near-surface "blind zone" (e.g., 1.2 km for CloudSat) (Maahn et al., 2014). In this context, ground-based vertical profilers provide a significant advantage by enabling high-resolution monitoring of atmospheric processes (Das and Maitra, 2016; Das et al., 2010; Maahn

* Corresponding author.
E-mail addresses: saurabh.das@iiti.ac.in, das.saurabh01@gmail.com (S. Das).

https://doi.org/10.1016/j.atmosres.2025.108531
Received 12 June 2025; Received in revised form 2 October 2025; Accepted 3 October 2025
Available online 6 October 2025

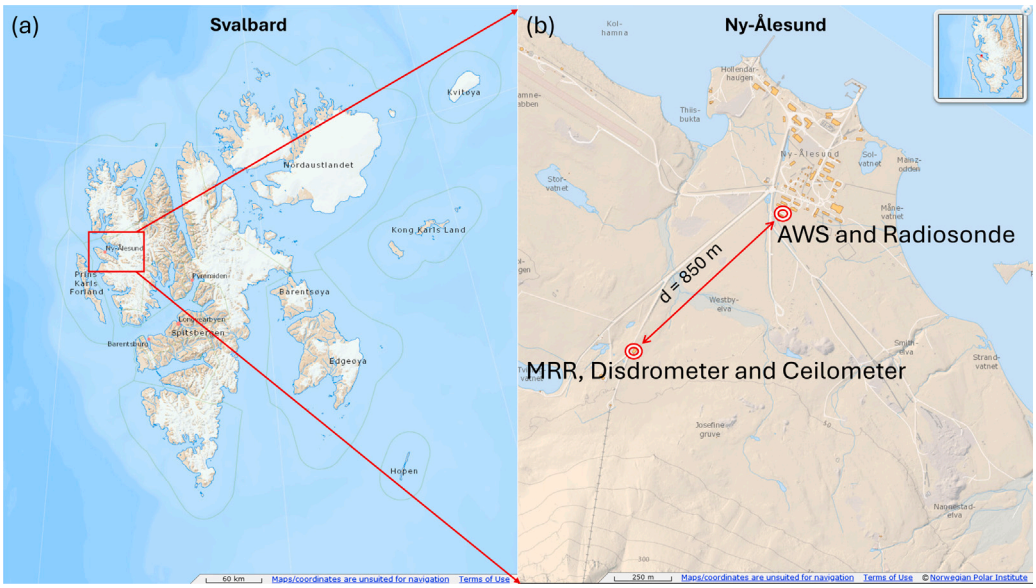

Fig. 1. Geographical location of Ny-Ålesund Research Station in (a) Svalbard, Arctic, showing two main atmospheric observation sites: (b) the Gruvebadet Atmospheric Laboratory, operated by the Indian Himadri Research Station, and the AWIPEV Research Station, jointly run by the German and French polar programs. The two observatory sites are approximately 850 m apart.
Source: (https://toposvalbard.npolar.no/)

et al., 2014). High resolution vertical profiles are expected to characterize different types of Arctic precipitation and can improve satellite-based quantitative precipitation estimation (QPE) (Schumacher and Houze Jr., 2006; Palerme et al., 2014; Casella et al., 2017). However, data from ground-based vertical precipitation profiles in polar regions are very limited, mainly due to harsh and logistically challenging environmental conditions.

This study presents a detailed investigation of various types of precipitation using a combination of ground observation with vertical profiles to track the evolution of precipitation at different altitudes. This is facilitated by experimental observations at the Himadri Research Station in Ny-Ålesund, Svalbard (74 ° -81 ° N), located on the primary pathway for the transport of atmospheric moisture into the Arctic (Serreze et al., 2007). The use of in-situ instruments become critical because of the region's unique climate sensitivity and the scarcity of reliable observations. These precipitation observations are further linked with meteorological profiles obtained from surface and radiosonde observations.

2. Site location

In-situ observational data were collected from the Himadri Research Station, situated in Ny-Ålesund (78 ° 55'N, 11 ° 56'E), Svalbard, Norway as shown in Fig. 1(a). Ny-Ålesund experiences relatively high tropospheric temperatures (Serreze et al., 2009; Maturilli and Kayser, 2017) and a coastal Arctic climate (Przybylak et al., 2003) located along the southern shore of Kongsfjorden fjord in Spitsbergen. The station is ~ 1231 km from the geographic North Pole, making it the northernmost inhabited research station in the world. The meteorological conditions of the region are strongly modulated by the surrounding orographic characteristics and the warm ocean (Maturilli and Kayser, 2017). This research station facilitates continuous atmospheric observation of clouds and precipitation using ground-based instruments. In this study, two observatory sites were utilized for data acquisition: the Gruvebadet Atmospheric Laboratory, operated under the Indian Himadri Research Station, and the AWIPEV Arctic Research Station, jointly managed by the German and French polar research programs. The two sites are located ~ 850 m apart in Ny-Ålesund as shown in Fig. 1(b).

3. Data and instruments

3.1. Instruments

Fig. 2 shows the instruments installed at the Gruvebadet Atmospheric Laboratory (Fig. 2(a)) and the AWIPEV research station. Micro rain radar (MRR), OTT Parsivel^2 disdrometer and ceilometer are installed at the Himadri site as shown in Fig. 2(b–d) respectively. Automatic Weather Station (AWS) and the radiosonde are operated at the AWIPEV site. The technical information on the instruments are detailed in Table 1.

3.1.1. Micro rain radar (MRR)

Vertical precipitation profiles captured using the MRR2 (METEK GmbH) as shown in Table 1(b), is a Frequency Modulated Continuous Wave (FM-CW) radar operating at 24 GHz (K band), producing 64-bin Doppler spectra at 32 vertical levels. Its high vertical (200 m) and temporal resolution (10 s) allow it to track the formation of the frozen hydrometeor, detect the melting layer as the bright band, and monitor the evolution of the hydrometeors across height ranges up to 6 km (Peters et al., 2002). It has a parabolic dish 0.5 m diameter fixed at a 63° angle with the vertical axis.

Two of its main limitations are the inability to distinguish between snow-rain particles and the presence of snow ice on the radar antenna. A 200 W dish heating system has been installed to avoid snow accumulation on the dish. The other inability of MRR to distinguish between snow and rain makes the instrument biased for liquid precipitation. To overcome this limitation in investigating the vertical evolution of Arctic precipitation, raw MRR data were processed for 1 min temporal resolution using the IMProToo algorithm developed by Maahn and Kollias (2012). This method significantly improves snowfall detection by applying advanced signal processing, dynamic dealiasing to handle velocity folding, and noise filtering that isolates the strongest Doppler signal peaks. The MRR was configured with a vertical resolution of 200 m at 32 altitude levels. To reduce ground clutter and instrumental noise, the lower and upper levels (0, 1, 2, and 31) were excluded, focusing the analysis between 600 m and 6 km altitude.

Table 1
Technical specifications of instruments used in this study.

Instruments /Parameter	OTT parsivel^2	MRR2	Ceilometer (CL51)	AWS	Radiosonde
Measurement Principle	Optical extinction of laser beam	Doppler radar (FMCW)	Backscatter from aerosols /clouds	In-situ sensors	Balloon -borne sensing
Measured Variables	Particle size (0.2–25 mm), fall velocity, Precipitation type and Intensity	Reflectivity, Doppler fall velocity, Spectral Width	Cloud base heights	Temperature, Wind, humidity, pressure	Profiles of Temperature, Humidity, Wind, Pressure
Frequency /Wavelength	780 nm	24.1 GHz	910 nm	NA	NA
Vertical Resolution	Surface	200 m	10 m	2/10 m	5–10 m(low)
Temporal Resolution	1 min	1 min	6 s	1 min	Daily
Detection Range	Surface	6 km	7.7 km	Surface	30 km

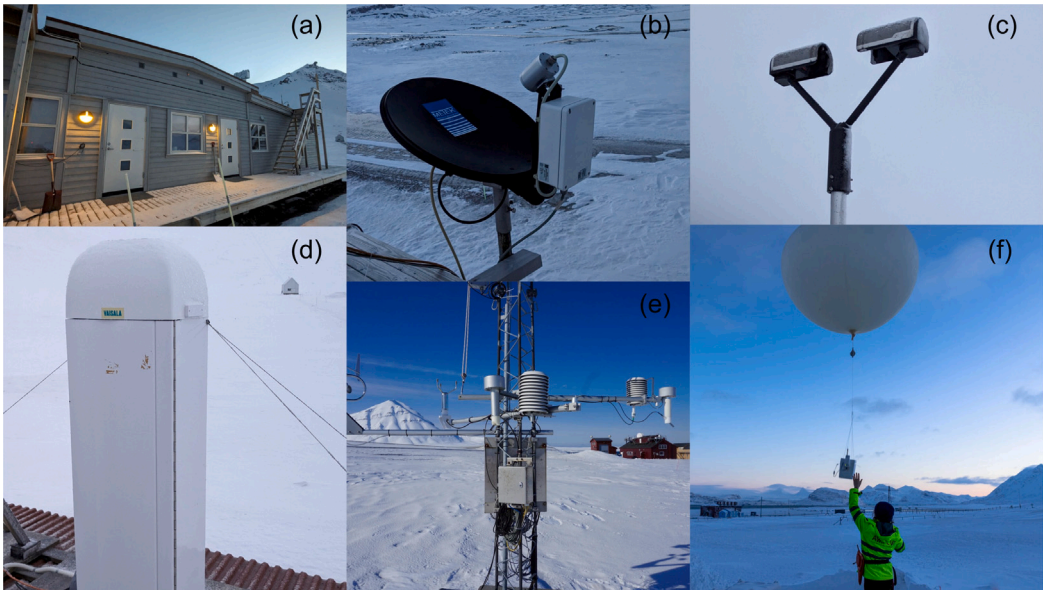

Fig. 2. The instrument site (a) Gruvebadet Atmospheric Laboratory facilitates continuous observations using (b) Micro Rain Radar, (c) disdrometer, and (d) ceilometer. The AWIPEV Research Station supports continuous measurements from (e) Automatic Weather Station (Source: https://www.awipev.eu/science/atmosphere-observatory/) and (f) daily tropospheric profiles using radiosondes.

3.1.2. OTT parsivel ^{2} disdrometer

The **Par**ticle **Si**ze and **Vel**ocity (Parsivel^2) optical disdrometer, manufactured by OTT GmbH, was used to observe surface precipitation (Löffler-Mang and Joss, 2000) (Fig. 2(c)). The disdrometer observed the hydrometers that cross the 1 mm horizontal laser beam of 780 nm with an area of 180 × 30 mm^2 between the disdrometer's transmitter and receiver heads. This measures hydrometeors with diameters of 0–25 mm and velocities of 0–22.4 ms^{-1} in 32 class bins (GmbH, 2025; Löffler-Mang and Joss, 2000).

The disdrometer provides valuable information about the hydrometeor size and the fall velocity near the ground independently. Disdrometer-derived particle size and fall velocity were further used to classify precipitation types between snow and rain. The hydrometeors were grouped according to varied diameter–velocity relationships, and dominant types (e.g., rain or snow) were identified over a 1 min interval (Löffler-Mang and Joss, 2000; GmbH, 2025). The precipitation intensity was further used to classify the types of precipitation according to the WMO guidelines (Jarraud, 2008). Disdrometer classify precipitation into the following types: snow (SN), rain (RA), rain with snow (RASN), drizzle (DZ), rain with drizzle (RADZ) and graupel/small hail (GS).

Parsivel^2 also has some limitations, including wind-induced tilting of particle trajectories that can bias fall speed and size retrievals (Battaglia et al., 2010; Sarkar et al., 2015). In strong winds, blowing snow from the ground can sometimes be mistaken for falling precipitation, especially during blizzards. To reduce noise and eliminate spurious signals, only periods with a precipitation intensity of 1 min exceeding 0.1 mmh^{-1} were considered for the analysis. The simultaneous falling of multiple particles through the laser beam may also result in false classifications or undercounting (Tokay et al., 2014). Moreover,

the assumption of spherical hydrometeors introduces uncertainties for nonspherical particles such as snow and graupel/hails (Löffler-Mang and Joss, 2000).

3.1.3. Ceilometer

The Vaisala CL51 ceilometer, which works on pulsed diode laser technology light detection and ranging (LIDAR) at 910 nm, is shown in Fig. 2(d). These upward traveling pulses are scattered back by particles such as haze, fog, mist, virga, precipitation, and clouds. The instrument measures this backscattered light to create a vertical profile of signal strength. By calculating the time delay between sending the pulse and receiving the backscatter, the ceilometer determines the cloud base height (CBH) (Source : https://docs.vaisala.com/r/M210801EN-K/en-US). The ceilometer was used to monitor CBH up to three layers, namely CBH1, CBH2, and CBH3 according to the cloud backscatter coefficient. CBH1 is the lowest cloud base, followed by CBH2 and CBH3. The ceilometer can detect the CBH1 quite well, but their limited range and attenuation of the signal inside thick clouds or during precipitation often limit the higher cloud base observations. The ceilometer has a vertical resolution of 10 m, a temporal resolution of 6 s, and a maximum range of 7.7 km (Oyj, 2022; Maturilli and Ebell, 2018). The ceilometer data files were averaged for a temporal resolution of 1 min.

3.1.4. Automatic weather station (AWS)

A meteorological mast or AWS located next to the AWIPEV Atmosphere Observatory provided continuous weather observations at Ny-Ålesund. Shaded and vented PT100 sensors were used to detect air temperature at 2 and 10 m, and a Combined Wind Sensor Classic (Thies Clima) was used to record wind direction and speed at the same elevations. Two separate humidity sensors monitored relative humidity at 2 m, while a barometer sensor placed about 10 m north of the tower recorded the station pressure. For the current study 2 m level data for all parameters with a temporal resolution of 1 min were used.

3.1.5. Radiosonde

Daily radiosonde observations by AWIPEV from Ny-Ålesund were taken once a day and processed by the Global Climate Observing System (GCOS) Reference Upper-Air Network (GRUAN). The GRUAN RS41-GDP1 processing algorithm applies corrections to systematic errors in the measurement of pressure, temperature, relative humidity, wind speed, and wind direction as detailed in GRUAN Technical Note TN-13 (available at www.gruan.org). In the current study, profiles of temperature, humidity and wind speed, up to 10 km have been used.

3.2. Data

To facilitate synchronized analysis, observational data from all ground-based instruments were resampled at the same temporal resolution of 1 min. Surface precipitation from the OTT Parsivel^2 disdrometer, vertical profiles of precipitation from MRR, cloud base height from the ceilometer, and ground-level meteorological parameters from AWS have been used for the period 2020–2024. For tropospheric meteorological conditions, radiosonde data (2017–2022) were collected from the AWIPEV research station (Maturilli, 2020; Maturilli and Dünschede, 2023). Table 2 shows the matched 1 min data samples of various instruments with the disdrometer for different types of precipitation in the respective columns.

Table 2
Number of 1-min sampled data points used for different parameters.

Type	Disdrometer	Micro Rain Radar	Ceilometer	AWS
SN	116,518	71,421	60,637	113,887
RA	41,737	29,041	31,069	41,737
RASN	1046	864	542	1046
DZ	4953	3703	4492	4953
RADZ	31,819	22,005	24,498	31,721
GS	6958	4248	3895	6917

4. Methodology

As already mentioned, the Parsivel^2 disdrometer categorizes precipitation into six different types, according to the relationship between the fall velocity and diameter of the particle. The study first analyzes the different types of surface observed precipitation and explores the meteorological conditions at 10 m. These include temperature, relative humidity, wind speed and surface pressure to explain the occurrence of different types of precipitation. For vertical precipitation structures, fundamental radar-retrieved parameters such as reflectivity (Ze), Doppler velocity (W), and spectral width (SW) have been used. Although these radar moments are not entirely capable of resolving microphysics, they provide useful insight about the physical processes. The particle size distribution (PSD) is not used here, as the retrieval of PSD for snow particles is not realistic with MRR because the shape and density of the snow particles vary widely and cannot be modeled adequately without these factors.

Ze is the backscattered power of the hydrometeors, which depends on their size and phase through the dielectric constant ($|K^2|$). Dielectric constant ($|K^2|$) depends on the radar frequency and the particle temperature (Boudala et al., 2025; Liebe et al., 1991). Notably, the higher dielectric constant ($|K^2|$) of the liquid particle reflects a more substantial signal compared to the solid particles (Suh et al., 2021; Atlas et al., 1973). Hence, Ze is essential for understanding the precipitation profile together with W, which plays a crucial role in understanding the complex vertical evolution of precipitation. W is influenced by various factors including particle size, vertical air movement and Reynolds number (Re) governed by air friction and air density (ρ_a) (Mitchell and Heymsfield, 2005; Heymsfield and Westbrook, 2010; Böhm, 1989). SW represents the variation in W at a certain level within the MRR sample volume induced by W variety, shear, and turbulence (Doviak and Zrnic, 2014). Here, SW combined with W helps to interpret the dynamical variability and microphysical processes within precipitation layers. Vertical evolutions were analyzed using Contour Frequency by Altitude Diagrams (CFADs) of Ze, W, and SW to explore the vertical development of different types of precipitation. Occurrences at different altitudes were compared with normalizing the CFAD values by dividing each bin count by the maximum count at that height. The distribution of cloud base heights (CBH1 and CBH2) associated with different precipitation types were also analyzed.

Since radiosonde profiles are only available once a day, instead of matching with precipitation profiles exactly at the same time, the study focused on the seasonal characteristics of atmospheric conditions. Accordingly, the vertical profiles of different types of precipitation have been broadly categorized into two major types, namely solid (including snow, graupel and mixed rain–snow events) and liquid (including rain, drizzle, and rain with drizzle). The seasons are defined according to the conventional meteorological classification: winter (December–February), spring (March–May), summer (June–August), and autumn (September–November). The seasonal CFAD profiles of temperature, humidity and wind speed up to 10 km generated from radiosonde observation were explored.

5. Results and discussion

The results are organized as follows: First, we discuss two case studies of dominant types, snow and rain, in detail, followed by the overall statistical analysis. The analysis is in two parts: first, the surface precipitation characteristics and associated meteorological conditions are analyzed. Furthermore, vertical precipitation structures and cloud base height are analyzed. Finally, seasonal variations of the vertical precipitation profile and associated meteorological profiles are discussed.

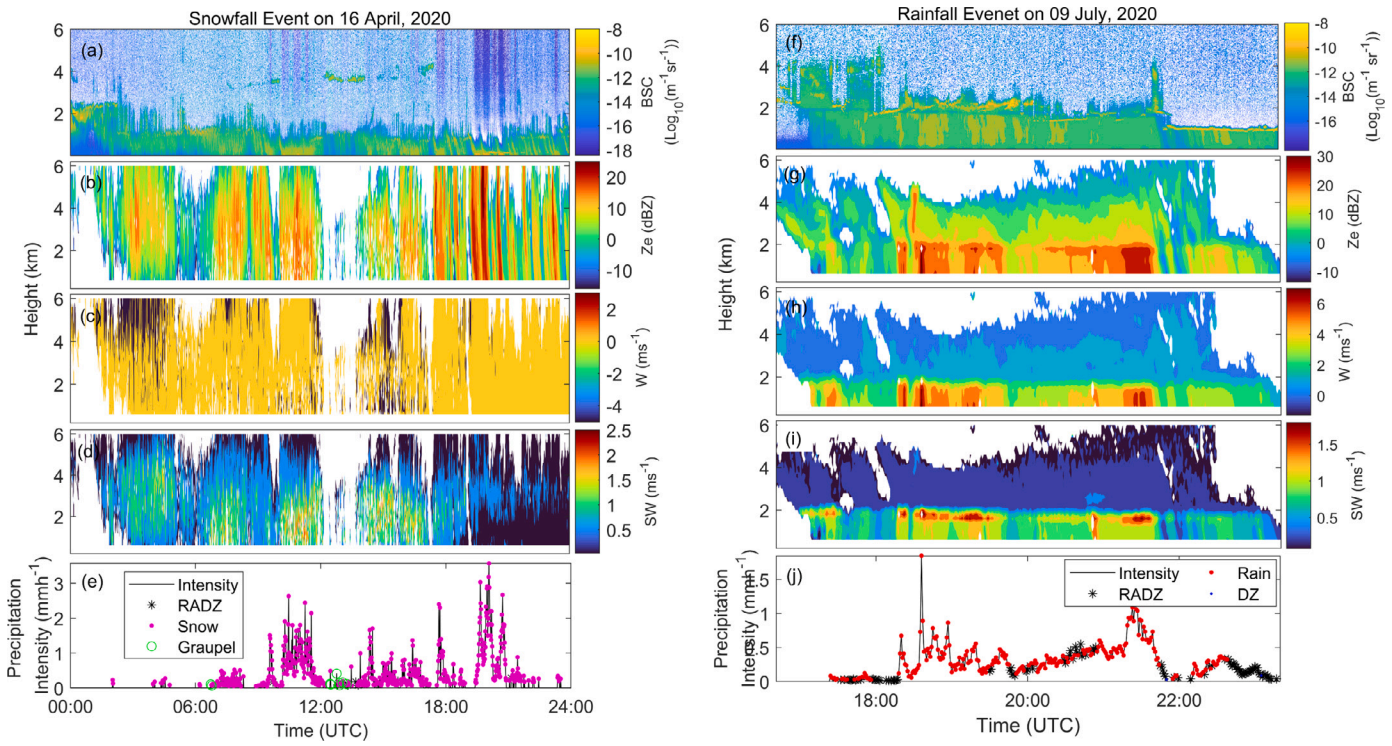

Fig. 3. Time–height profiles of atmospheric and surface observations during two distinct precipitation events: (a–e) snow event on 16 April and (f–j) rain event on 9 July, 2020. Panels show (a, f) cloud backscattered coefficient from ceilometer, (b, g) radar reflectivity (Ze), (c, h) Doppler fall velocity (W), and (d, i) spectral width (SW) from the Micro Rain Radar (MRR) up to 6 km along with (e, j) precipitation intensity from the disdrometer.

5.1. Case studies of snow and rain

Two different precipitation events are presented in Fig. 3(a–e) and (f–j). On 16 April 2020, a 18 hour long snowfall event was observed and on 9 July 2020, a 5 hour long rain event was recorded, respectively, as shown in Fig. 3(e,j). It can be seen that the SN event was associated with a lower cloud base (~1 km) compared to the RA ~ 2 km (Fig. 3(a,f)). During snowfall, a uniform vertical profile of Ze was observed along with uniform W and SW, indicating a consistent distribution of snow particle size across height ranges (Fig. 3(b–d)). The rain event, on the other hand, showed a sudden change in Ze, W and wider SW, especially below 2 km, suggesting the presence of a melting layer at this height with increased particle size (Fig. 3(g–i)). CFAD of different radar moments of these two events are shown in Fig. 4. The SN event shows an almost uniform Ze and W, except for a small jump around 3 km. It coincides with an increase in SW at an altitude of 3 km, suggesting an increase in turbulence or a different microphysical process leading to the formation of particles of different sizes and subsequent variation in W. This region most likely indicates the start of the snowfall regime. Rain, on the other hand, shows a gradually increasing Ze with a decrease in height and a sudden enhancement around 2 km. The W also shows two distinct peaks around 3 km and 2 km. The increase in both W and Ze around 2 km indicates the presence of a melting layer below which the rain exists and above which the snow exists. The other peak on the W indicates the region from which snowfall starts. The SW changes at two distinct heights, corresponding to the within-cloud and rain region turbulence.

To better understand the characteristics of the above mentioned features in this region, statistical evaluations combining all the events observed during 5 year periods were carried out next.

5.2. Statistical analysis

5.2.1. Observed precipitation types and meteorological conditions at ground

Precipitation characteristics. The precipitation classification considered in this paper is based on the observation of the disdrometer. Saini et al. (2025) reported that SN is the most frequent, followed by RA and other types of precipitation in this location. Their seasonal occurrence and associated precipitation rates are presented here using bar (left y-axis) and violin (right y-axis) plots, respectively, in Fig. 5(a–f). Spring shows the highest occurrence of SN (~ 40%), followed by winter and autumn, with the lowest frequency observed during summer. Notably, snow intensity reaches up to ~4 mmh^{-1} with the highest occurrence around ~ 1.5 mmh^{-1} in winter and around ~ 0.5 mmh^{-1} in other seasons. RA occurs predominantly (~ 50%) in summer, followed by autumn and spring, with the lowest occurrence in winter. RA generally has lower intensities compared to snow, with the majority of occurrences around ~ 0.4 mmh^{-1}. Mixed-phase precipitation RASN occurs predominantly during the transitional spring season, followed by summer, autumn, and winter with higher intensity compared to RA and SN. However, its annual occurrence remains low compared to SN and RA, as reported by Saini et al. (2025).

Both DZ and RADZ, which are forms of liquid precipitation, occur primarily during the summer, followed by transitional seasons with the least in winter. GS occurrences are distributed throughout the year, with a higher presence during spring. The precipitation rate associated with the GS is generally comparable to that of the SN during all seasons, except during winter, when the GS shows considerably lower intensities.

Meteorological conditions. To understand the meteorological conditions associated with the different types of precipitation, the corresponding 2 m temperature, relative humidity, wind speed, and surface pressure were next studied and presented in Fig. 6(a–d), respectively. SN occurs predominantly near 0 °C temperatures, with more than half of the cases occurring below 0 °C, favoring the ice phase, as shown in Fig. 6(a). Meanwhile, all other types of precipitation occur primarily above freezing conditions. DZ and RADZ display a bimodal temperature distribution, suggesting a strong temperature dependence. RA events peak around 3 °C, aligning with typical warm-phase conditions. GS is often associated with convective and riming processes and shows a peak

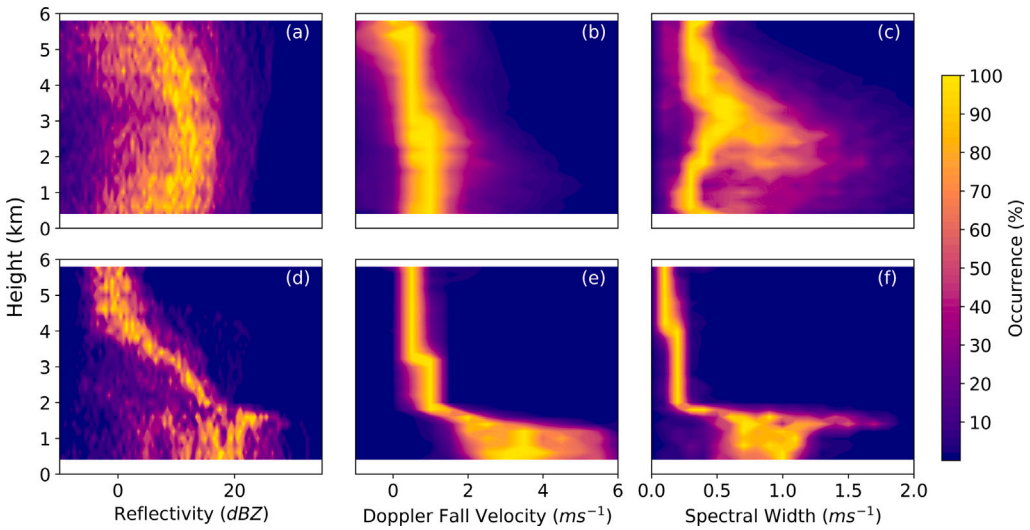

Fig. 4. CFAD profiles for snow (a–c) and rain (d–f) events, showing vertical distributions up to 6 km of (a, d) radar reflectivity (Ze), (b, e) Doppler fall velocity (W), and (c, f) spectral width (SW).

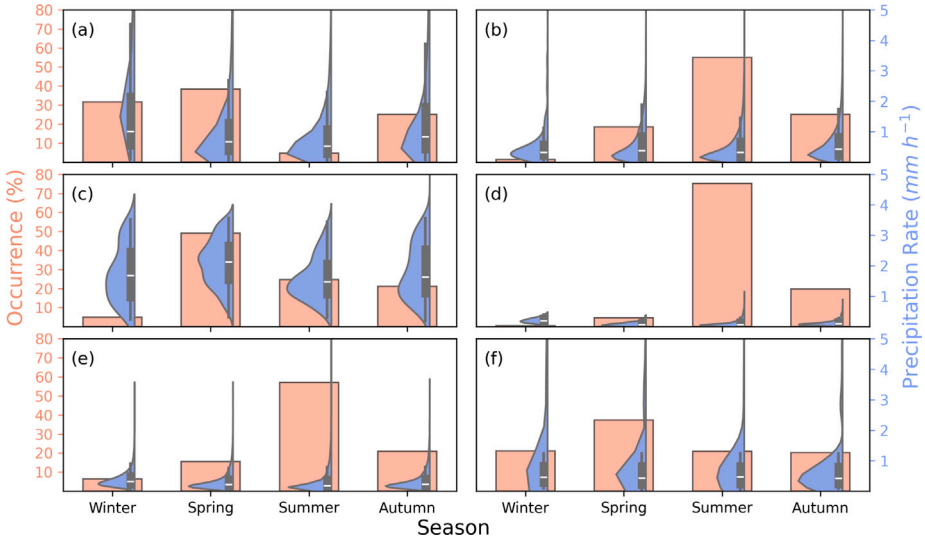

Fig. 5. Seasonal occurrence (bar) and intensity distribution (violin plot) of different precipitation types observed at Ny-Ålesund, Svalbard: (a) snow, (b) rain, (c) rain–snow mix, (d) drizzle, (e) rain with drizzle, and (f) graupel. The bars represent the frequency of occurrence, while the violin plots illustrate the distribution and variability of precipitation intensity across each season.

near 1 °C, indicating the possibilities of the presence of supercooled liquid water and mixed-phase microphysics at higher heights.

From Fig. 6(b), it can be seen that all precipitations are associated with high relative humidity, typically exceeding ~ 65%. Liquid precipitation, including RA, DZ and RADZ occurs primarily at RH above 75%, with peak values around 95%, 85%, and 90%, respectively. Mixed-phase RASN shows comparatively lower RH values. Solid precipitation SN and GS show wider RH distributions, with peaks ranging 80%–90%. As shown in Fig. 6(c), liquid and mixed precipitation are generally associated with moderate wind speeds, predominantly below 5 ms^{-1}, indicative of relatively stable stratiform environments. RA and RADZ exhibit lower wind speeds, peaks between 1–2 ms^{-1}, characteristic of weakly forced systems. In comparison, SN and GS show broader wind speed distributions with >10 ms^{-1}, consistent with dynamically active or convective conditions (Liu et al., 2013).

As shown in Fig. 6(d), SN and GS occur in a broad range of pressure (~ 980–1010 hPa), indicating dynamic active conditions (Gevorgyan et al., 2022). RA, DZ, RASN and RADZ occur at higher pressures (~1000–1010 hPa), indicating stable stratiform conditions.

5.2.2. Vertical profiles of precipitation and atmospheric parameters

Vertical profiles of different precipitation types. To understand the vertical evolution of precipitation during different types Fig. 7, Fig. 8 and Fig. 9 presents the CFAD of Ze, W, and SW, respectively. For snow, Fig. 7(a) shows a wide Ze range, with a reflectivity of maximum occurrence increases towards ground but with a lower rate below ~ 1.5 km. The occurrence of W is mostly below 2 ms^{-1} (Fig. 8(a)) throughout the height ranges. However, SW suddenly increases below ~ 1.5 km significantly (Fig. 9(a)). Low W values reflect slowly falling particles, most likely low-density snowflakes with large surface areas (Locatelli and Hobbs, 1974; Fitch et al., 2021; Garrett et al., 2012). The increase in Ze with low W and low SW profiles at higher heights indicates stratiform snowfall regimes, dominated by deposition and aggregation under relatively stable and weakly turbulent conditions above ~ 1.5 km (Grazioli et al., 2017; Field and Heymsfield, 2003). The almost uniform Ze profiles, along with high SW at lower height, indicate a wide distribution of particle size but a uniform vertical variation in the boundary layer.

For RA, the Ze profile shows a steadily increasing value towards the surface, as shown in Fig. 7(b). A slight change in the Ze slope is

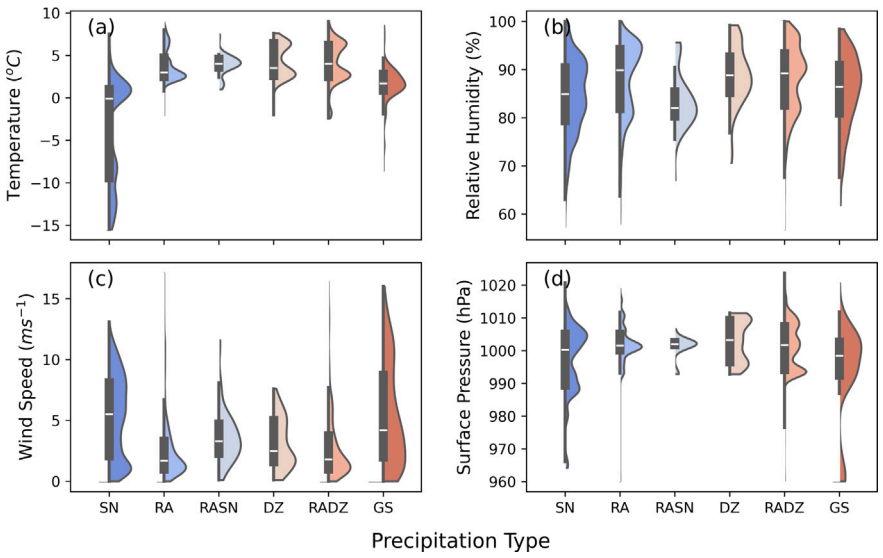

Fig. 6. The violin distributions of 2 m meteorological parameters (a) temperature (°C), (b) relative humidity (%), (c) wind speed (ms^{-1}), and (d) surface level pressure (hPa) are examined in relation to different precipitation types observed at Ny-Ålesund.

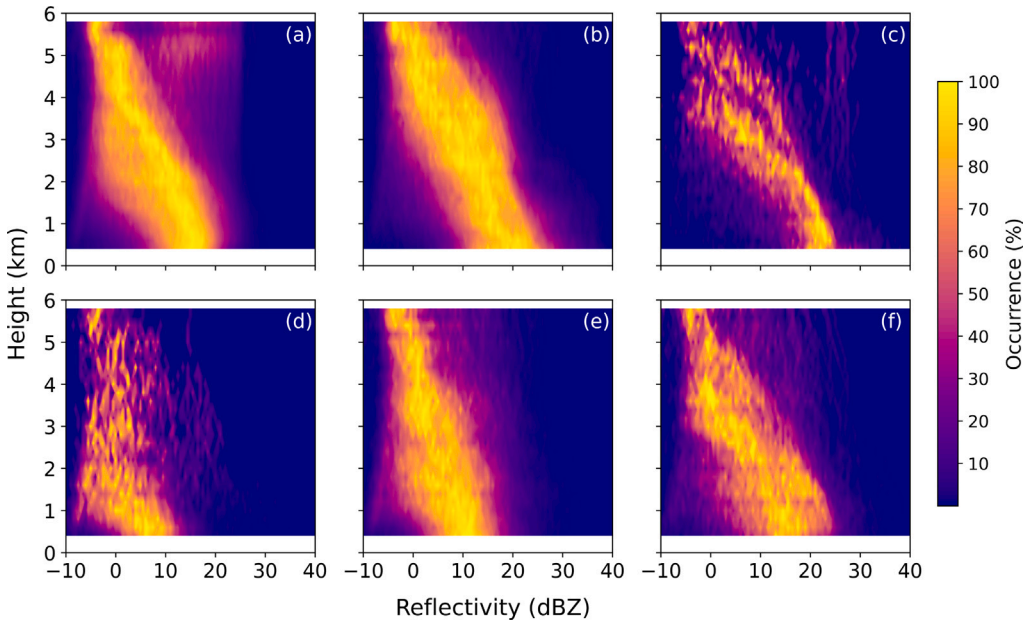

Fig. 7. CFAD of reflectivity (Ze) up to 6 km for different precipitation types: (a) snow, (b) rain, (c) rain with snow, (d) drizzle, (e) rain with drizzle, and (f) graupel.

observed around ~1.5-2 km altitude, an indication of the presence of a melting layer where the ice particles transform into liquid (Allabakash et al., 2019; Wolfensberger et al., 2016). Below this layer, Ze continues to increase, reaching ~30 dBZ near the surface. Interestingly, W below the melting layer at 2 km also increases compared to SN and shows peak occurrences that exceed 6 ms^{-1} near the surface, as shown in Fig. 8(b), indicating liquid precipitation. The SW profile shown in Fig. 9(b) also indicates a significantly higher enhancement at lower altitudes, particularly below 2 km, reaching values > 1.5 ms^{-1}. This, along with the large Ze, suggests the formation of larger raindrops due to the collision coalescence process below the melting layer (Bringi and Chandrasekar, 2001; Beard and Ochs III, 1993) with a substantial particle size diversity, leading to a wide distribution of W.

RASN, a mixture of wet snow and rain, occurs when near-surface air is slightly warmer than freezing (Society, 2025) also seen in Fig. 6. Ze profile in Fig. 7(c) shows low values above ~2 km with low W (Fig. 8(c)) and SW (Fig. 9(c)) indicating the snow regime. A broad range of reflectivity with increasing W and a small but noticeable jump in SW around 3-4 km indicate a mixture of snow, melted snow and probably also rain at that height (Fabry and Zawadzki, 1995). A significant jump in SW, along with high W and Ze can be seen around 2 km and below. However, the range of Ze becomes narrower than above height. This indicates a narrow PSD with the peak of PSD towards the high end.

DZ shows low Ze values (<15 dBZ) in Fig. 7(d), with a slight increase below ~2 km, consistent with a melting layer (Fabry and Zawadzki, 1995). Lower Ze values indicate small droplets and low liquid water content (Bringi and Chandrasekar, 2001). W profile in Fig. 8(d) shows low and uniform (<2 ms^{-1}) values suggesting homogeneous small drops (Beard and Ochs III, 1993; Bringi and Chandrasekar, 2001). The SW in Fig. 9(d) remains comparably narrow (<1 ms^{-1}), reflecting weak variability in W (Shupe et al., 2005). These features may originate

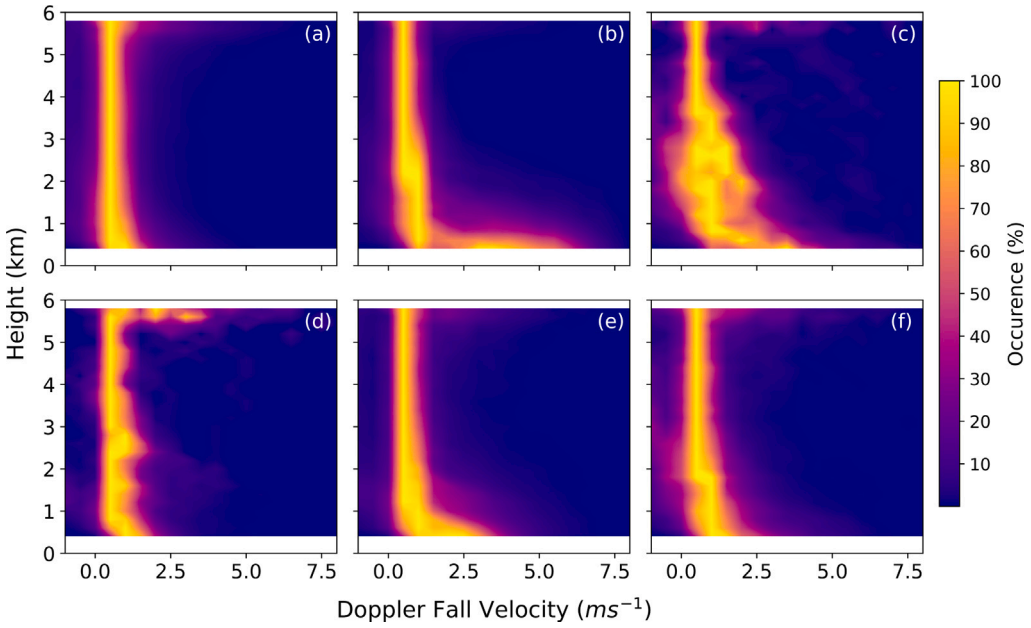

Fig. 8. CFAD of Doppler fall velocity (W) up to 6 km for different precipitation types: (a) snow, (b) rain, (c) rain with snow, (d) drizzle, (e) rain with drizzle, and (f) graupel.

from shallow stratiform clouds with limited coalescence and turbulence that produce small droplets (Wood, 2005; Huige et al., 2024).

During RADZ events as shown in Fig. 7(e), the profiles are intermediate between RA and DZ. At higher levels, Ze remains weak, consistent with DZ, but increases sharply near the surface with a maximum ~20 dBZ. This pattern reflects the presence of small drops at higher altitude, but grows into larger raindrops with the coalescence process (Beard and Ochs III, 1993). In Fig. 8(e), W shows an intermediate range (~1–4 ms^{-1}), indicating a mixture of particle sizes of RA and DZ. The SW profile in Fig. 9(e) also shows a moderate increase near the surface, up to 1.5 ms^{-1}, suggesting a wider distribution of particle sizes. These features highlight a transition stage, where DZ evolves into RA within a moist and mildly turbulent boundary layer (Wood, 2005; Huige et al., 2024).

GS shows a snow-like pattern but with higher Ze values (~5–30 dBZ) near the surface as shown in (Fig. 7(f)). The CFAD profile (Fig. 8(f)) shows elevated W (3–5 ms^{-1}) across all heights, consistent with rimed particles that are denser and fall faster than snow, but slower than RA (Hara et al., 2024; Pruppacher et al., 1998). Similar features were reported in an SN–GS transition case by Saini et al. (2025). The SW profile (Fig. 9(f)) reaches ~2 ms^{-1}, indicating a strong variability in the mass, shape and speed of the particle, likely driven by intense riming or updrafts within mixed-phase clouds (Oue et al., 2015; Pruppacher et al., 1998; Shupe et al., 2005).

Cloud base height. The ground-based LIDAR ceilometer provides the CBH associated with various types of precipitation. Fig. 10 shows the CBH1 and CBH2 that reveal the presence of single and double layer cloud structures, respectively. Observations of a third cloud base height (CBH3) were negligible at this site during the study period, indicating that the detected cloud systems were limited to a maximum of two layers. This may be because the study considers only the cloud base information during precipitation, which attenuates the signal much faster compared to non-precipitation situations. In Svalbard, periods of intense precipitation are often accompanied by high cloud bases (Nuncio et al., 2023, 2022). Fig. 10 indicates that precipitation events were predominantly associated with single-layered clouds, with an occurrence greater than 90%. It is to be noted here that the ceilometer cannot give the full cloud structure and, due to the limitation of LASER attenuation, the multi-layer clouds can only be detected if the first cloud layer is optically thin. Nonetheless, liquid-phase precipitation (RA, DZ and RADZ) showed a comparatively higher association with double-layered cloud structures than solid-phase precipitation (SN, RASN and GS).

The association of clouds with different types of precipitation can be better understood with the distribution of CBH1 and CBH2 occurrences at various altitudes, as shown in Fig. 11. During snowfall events (Fig. 11(a)), the CBH occurrences show a broad vertical spread starting from near the surface to ~ 2 km. The occurrence of CBH1 peaks around 0.5 km with CBH2 occurrences near 0.7 km indicating the presence of low-medium level ice-phase cloud layers. For RA events in Fig. 11(b), the CBH distribution is comparatively wider, spanning from the near surface to ~3 km. The CBH1 occurrences peak near ~ 0.7 km, while in the case of CBH2, it peaks close to 1 km. Elevated CBH2 occurrence reflects the presence of vertically extended liquid phase clouds, which facilitates warm-rain microphysics through collision–coalescence processes (Gupta et al., 2023). During RASN precipitation, as shown in Fig. 11(c), the range of CBH1 and CBH2 is confined below 1.6 km, with a primary peak similar to snow. The DZ producing cloud in Fig. 11(d) shows the lowest CBH1 and CBH2 values, generally peaking between 0.5 and 0.6 km. This limited vertical distance from the ground favors the formation of small droplets (Rangno, 2015).

RADZ in Fig. 11(e) displays an intermediate CBH profile, with a higher distribution than DZ but narrower than RA. The occurrences of CBH1 peaks near 0.6 km, while CBH2 ranges from 0.8 to 1 km. This indicates the presence of layered cloud systems, with shallow DZ layers with deeper rain-bearing clouds. Lastly, graupel precipitation in Fig. 11(f) shows a low-level presence of CBH1 similar to snow, while CBH2 displays a wider vertical spread extending up to 3 km. The in-cloud process may favor the formation of graupels due to the presence of different types of cloud at two different altitudes.

Seasonal variability of vertical profiles for liquid and solid precipitation. To understand the impact of atmospheric parameters on the vertical evolution of precipitation, the seasonal variability is studied next. The profiles of atmospheric parameters are taken from radiosonde observations, which were measured only once a day in the Arctic. Hence, the precipitation classes were regrouped into two major precipitation types: solid (SN, RASN and GS) and liquid (RA, DZ and RADZ). Seasonal variations of the vertical profiles of Ze, W, and SW are shown in Fig. 12, Fig. 13 and Fig. 14.

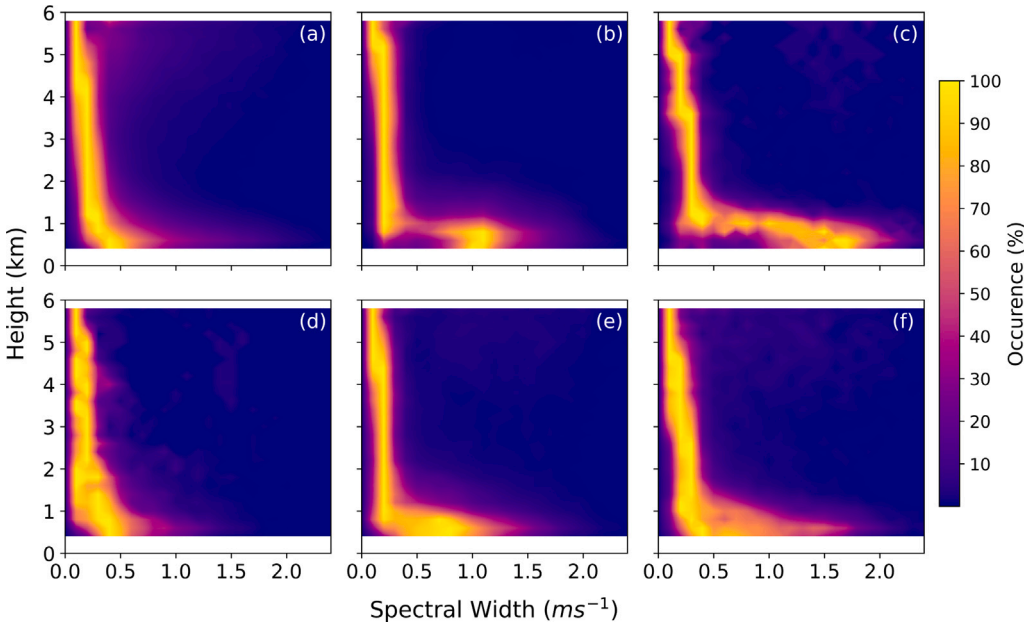

Fig. 9. CFAD of spectral width (SW) up to 6 km for different precipitation types: (a) snow, (b) rain, (c) rain with snow, (d) drizzle, (e) rain with drizzle, and (f) graupel.

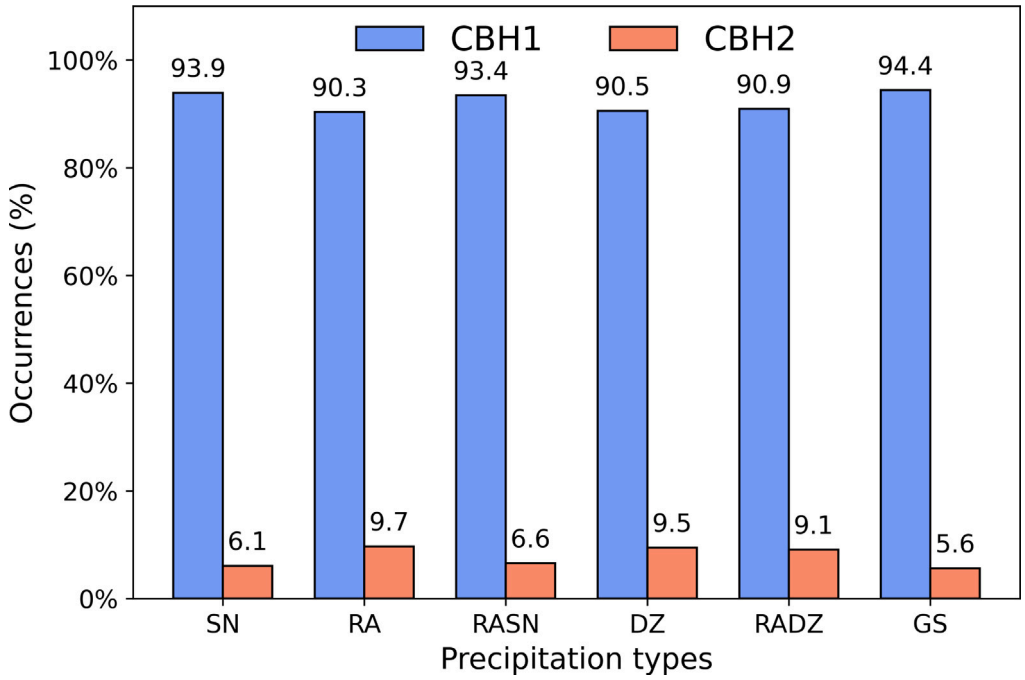

Fig. 10. Occurrence of CBH1 and CBH2 for different precipitation types, classifying single- and double-layered clouds.

The CFAD of Ze for liquid precipitation (Fig. 12(a–d)) shows a vertically extended structure up to 5–6 km across all seasons, with a distinct enhancement below ~ 2 km likely suggesting the presence of a melting layer (Fabry and Zawadzki, 1995). Interestingly, liquid precipitation shows the highest W (up to ~ 7 ms^{-1}) in winter, followed by autumn, summer and spring, accompanied by broader SW values below the melting layer.

In comparison, solid precipitation shows the highest vertical extent in winter, with Ze profiles extending up to ~6 km but lower near-surface reflectivity than liquid precipitation. Summer exhibits the weakest and shallowest Ze profiles (<4 km) due to the limited occurrence of solid precipitation. In general, the solid phase maintains a relatively lower seasonal variability in W compared to liquid precipitation. However, a higher W in spring and summer reflects partially melted hydrometeors due to the higher occurrence of RASN as observed in Fig. 5. Throughout all seasons, SW increases near the surface irrespective of the type of precipitation, pointing to boundary layer processes and turbulence near the ground, which leads to a wide particle size and speed (Boudala et al., 2025; Zhou et al., 2024; Durán Alárcon, 2019).

Seasonal variation of vertical profiles of meteorological parameters. Seasonal variations in vertical atmospheric parameters were analyzed next from radiosonde observations, as shown by CFAD profiles in Fig. 15, to understand the observed changes in precipitation types.

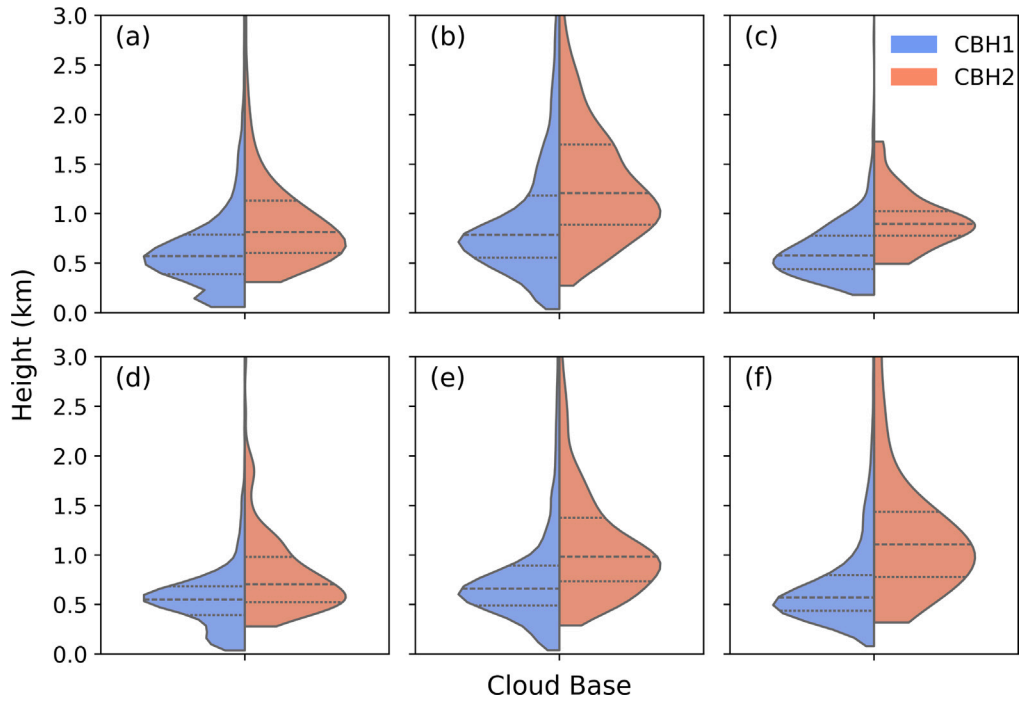

Fig. 11. Violin plots of CBH1 and CBH2 height distributions associated with different precipitation types: (a) snow, (b) rain, (c) rain with snow, (d) drizzle, (e) rain with drizzle, and (f) graupel.

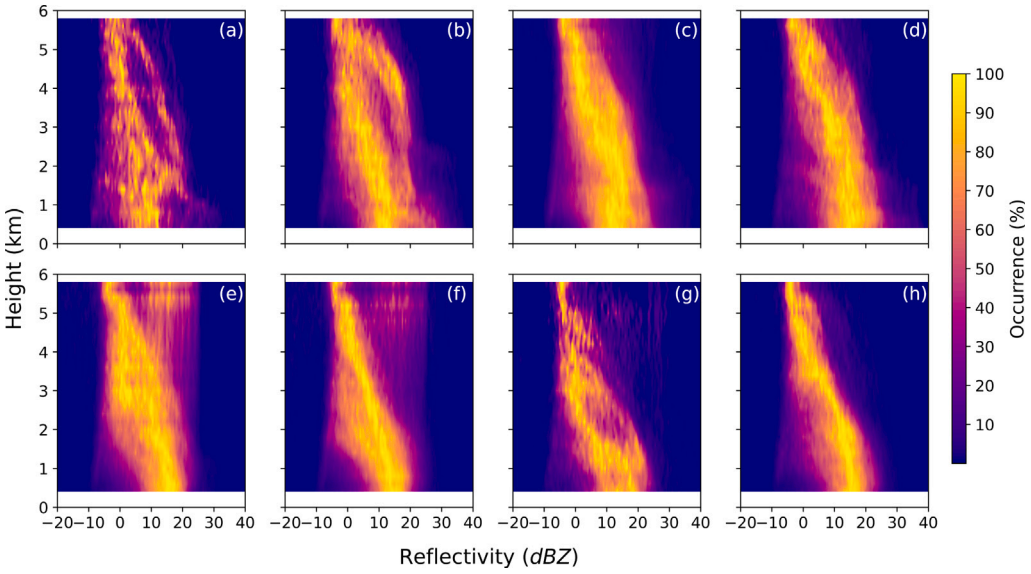

Fig. 12. Seasonal CFAD profiles of reflectivity (Ze) for (a–d) liquid-phase (rain, drizzle, rain–drizzle) and (e–h) solid-phase (snow, graupel, rain–snow) hydrometeors up to 6 km altitude during winter, spring, summer, and autumn, in columns respectively.

The rows represent the seasons: winter, spring, summer and autumn, whereas each column corresponds to the meteorological parameter: temperature, relative humidity, and wind speed, respectively.

The CFAD of temperature in Fig. 15(a,d,g,j) shows a narrower range during the summer season compared to other seasons. During winter, the temperature often remains below 0 ° C in all heights, but in spring and autumn shows a slight warming near the surface. Summer mostly shows above freezing level temperature at the surface extending up to 2 km. In the 0–10 km profile, mean lapse rates of 5-6 ° Ckm^{-1} are weaker than the dry adiabatic value (9.8 ° Ckm^{-1}) but in the range of the moist adiabatic range (~ 4–7 ° Ckm^{-1}) (Wallace and Hobbs, 2006) for all seasons. This suggests a conditionally unstable troposphere that can favor convection and precipitation when adequate moisture is present. On the other hand in 0-2 km boundary layer, lapse rate found to be weaker (3–5 ° Ckm^{-1}), often close to or below the moist adiabatic lapse rate, indicating a more stable or weakly unstable near-surface layer, particularly in summer (3.6 ° Ckm^{-1}).

Relative humidity, as shown in Fig. 15(b,e,h,k) follows a broadly similar vertical pattern throughout the seasons, increasing from drier conditions at higher altitude to nearly saturated levels near the surface. An increase in humidity below 4-6 km suggests a favorable environment for cloud formation within this layer. During summer and autumn, the saturated layer extends up to around ~6 km, whereas in winter and spring it remains confined below ~4 km. This may suggest that the height of cloud formation and precipitation varies season by season due to the moisture availability. Wind speed typically decreases with

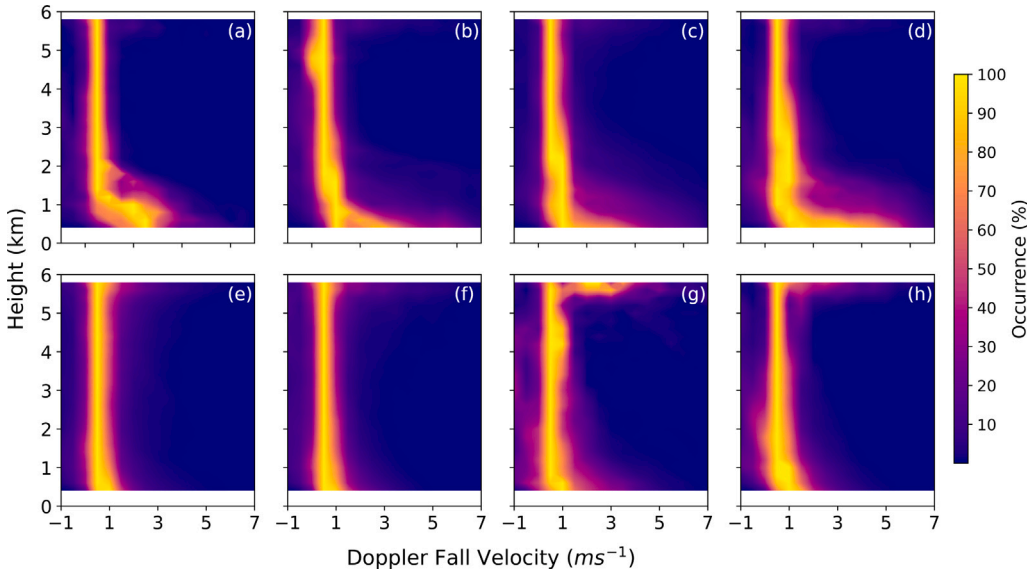

Fig. 13. Seasonal CFAD profiles of Doppler fall velocity (W) for (a–d) liquid-phase (rain, drizzle, rain–drizzle) and (e–h) solid-phase (snow, graupel, rain–snow) hydrometeors up to 6 km altitude during winter, spring, summer, and autumn, in columns respectively.

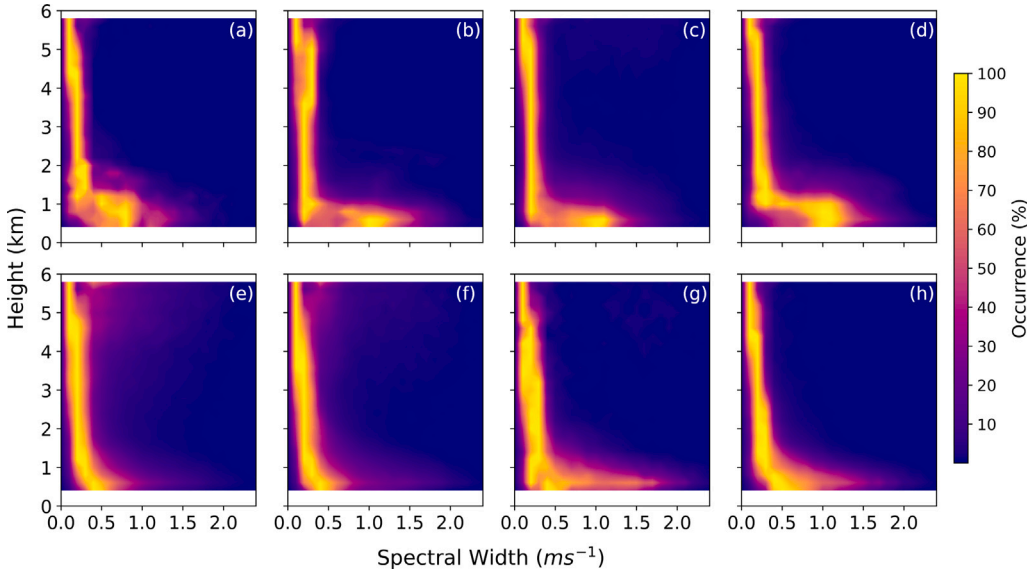

Fig. 14. Seasonal CFAD profiles of spectral width (SW) for (a–d) liquid-phase (rain, drizzle, rain–drizzle) and (e–h) solid-phase (snow, graupel, rain–snow) hydrometeors up to 6 km altitude during winter, spring, summer, and autumn, in columns respectively.

height, ranging from 0 to ~ 40 ms^{-1} as shown in Fig. 15(c,f,i,l). Near the surface, summer records the weakest winds, mostly below ~ 7 ms^{-1}, while the other seasons tend to show stronger surface winds, reaching up to ~ 10 ms^{-1}.

The general meteorological conditions highlight two key regions of interest. The first region is above 2 km up to 4–6 km, where cloud formation and precipitation begin, as reflected in the relative humidity profile. The second is below 2 km, highlighting both the melting layer and the boundary layer, where the atmosphere becomes warmer, particularly during the summer season, and humidity often reaches saturation. From this region, most precipitation begins to fall, as seen in Fig. 8.

6. Summary and conclusions

Precipitation is an important factor in the Earth's energy balance, water cycle, climate and the agricultural systems. In tropical regions, frequent and intense rainfall occurs due to strong convection and high moisture from nearby warm oceans (Houze, 2012). However, in higher latitude regions, such as the Arctic region, conditions are very different. Local convection is minimal, and most precipitation is driven by moisture transported from lower latitudes through large-scale atmospheric circulation (Jakobson and Vihma, 2010). This requires a better understanding of the vertical evolution of the precipitation process for different types of precipitation in the Arctic region.

In the present study, ground-based observations were used to study the vertical evolution of precipitation and associated meteorological conditions. Himadri Research Station in Ny-Ålesund, Svalbard, plays a key role in facilitating these atmospheric observations in the Arctic.

Arctic experiences different types of precipitation, including rain and snow (Saini et al., 2025). Mixed-phase precipitation was found to occur with the highest precipitation rates, followed by snow, graupel, and liquid forms in all seasons. Liquid precipitation typically occurs under warm and humid conditions, often accompanied by low wind

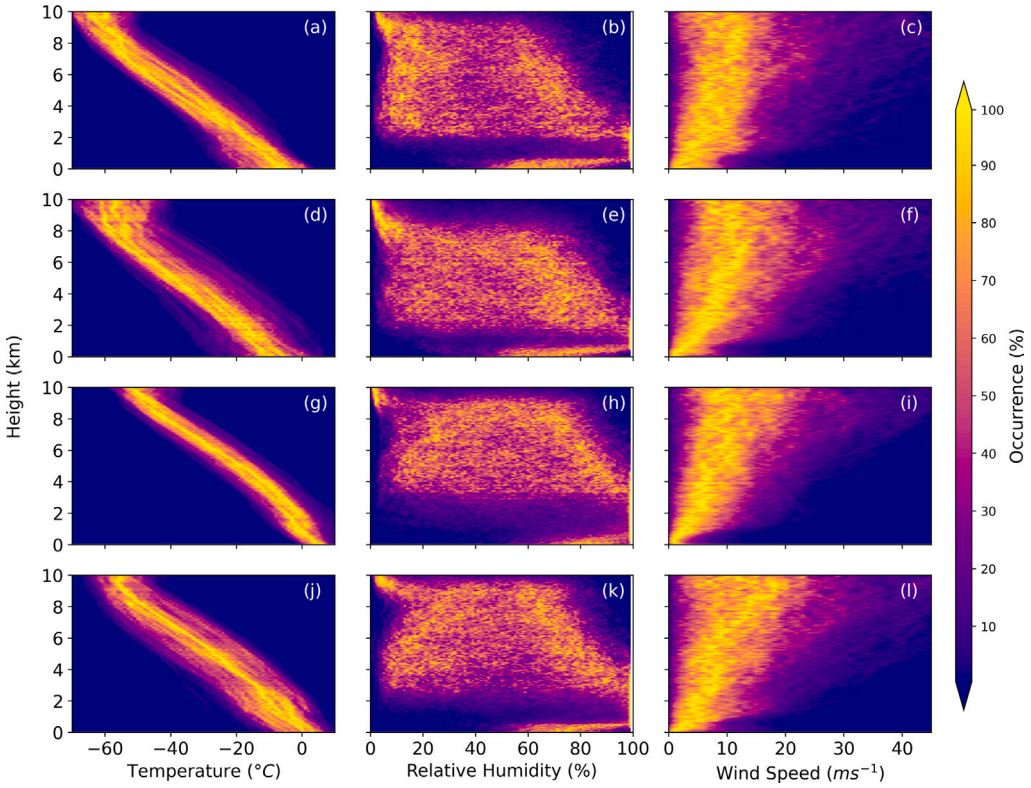

Fig. 15. Seasonal variation of CFAD profiles up to 10 km from radiosonde observations, showing vertical distributions of temperature (°C), relative humidity (%), and wind speed (ms^{-1}). Columns represent different variables, while rows correspond to the four seasons: winter, spring, summer, and autumn.

speeds and surface pressure. The summer profile of temperature and humidity favors the occurrence of liquid precipitation in a warm atmosphere. Liquid and mixed precipitation was also found to be associated with a comparably higher presence of double-layered clouds and higher cloud bases compared to solid-phase precipitation, consistent with previous observations of the vertical structure of the Arctic and global cloud (Intrieri et al., 2002; Nuncio et al., 2022).

Since PSD retrieval for solid phase precipitation is not possible without the knowledge of exact shape and density of the particle, this study explored vertical profiles of Ze, W and SW to understand the vertical evolution of different precipitation types. During SN, an increase in Ze with low W and SW above ~2 km indicates stratiform snowfall with deposition and aggregation under stable and weakly turbulent conditions (Grazioli et al., 2017; Field and Heymsfield, 2003). In contrast, below 2 km, the Ze profile becomes uniform with high SW near the surface, reflects broad but uniform particle size distributions along with turbulence throughout the boundary layer.

RA shows a sudden increase in the W (~7 ms^{-1}) and Ze (35 dBZ) below 2 km suggesting the presence of a melting layer. RA is also associated with high SW, suggesting that particle size variability leads to a wider distribution of W. The temperature profiles indicate the zero degree isotherm height around 2 km in summer supporting the detection of the melting layer at that height. The humidity profile also shows significant changes around that height, indicating the change in the phase of precipitation at that height.

Mixed-phase precipitation indicates the intermediate phase of snow and rain. Graupel, on the other hand, has the similar Ze of SN but an enhanced W with wide SW, signifying high fall velocity associated with larger sizes throughout the height ranges. This may be due to the riming process, as the temperature above 2 km is always below zero degree with sufficient availability of moisture across all seasons as seen from the relative humidity and temperature profiles.

Overall, the study points to two major vertical levels where the vertical evolution and microphysical processes change in the Arctic. Around 1.5–2 km, the presence of a zero degree isotherm (particularly in summer) facilitates the snow to rain transition (Saini et al., 2025). This is associated with the climatic feature of Ny-Ålesund as moisture transport also occurs mainly in the lower troposphere, up to ~850 hPa (~ 1.5 km), in the Arctic (Dorff et al., 2024). The boundary layer region below 1.5-2 km also shows a distinct vertical evolution that may be due to the increase in turbulence in all seasons. The other important height level is observed around 4 km above which again the profiles change significantly. The cloud to precipitation transition in this region may lead to these changes.

The study emphasizes the importance of using the high-resolution, ground-based observations in the high latitude arctic region to capture the vertical and seasonal variability of the Arctic precipitation profile. The outcomes are expected to improve satellite based precipitation estimation especially in the polar region.

CRediT authorship contribution statement

Lekhraj Saini: Writing – review & editing, Writing – original draft, Methodology, Investigation, Formal analysis, Conceptualization. **Saurabh Das:** Writing – review & editing, Supervision, Methodology, Funding acquisition, Conceptualization. **Nuncio Murukesh:** Writing – review & editing, Supervision, Data curation.

Declaration of competing interest

The authors declare that they have no known competing financial interests or personal relationships that could have appeared to influence the work reported in this paper.

Acknowledgments

The authors acknowledge the support provided by the Director of ESSO - NCPOR for Research in Svalbard (RiS ID 12263 and 12301) and

facilitating access to the essential data during this study (J-45/2025-26). The first author (LS) thanks the CSIR for the fellowship funding (09/1022(12356)/2021-EMR-I). One of the authors (SD) acknowledges the financial support provided by SERB, India (CRG/2022/006986) and MoES, India (MoES/16/4/2021-RDESS/NARM-4). Authors also acknowledges the AWIPEV research facility for providing the AWS and radiosonde data.

Data availability

Meteorological data from the Automatic Weather Station (AWS) and radiosonde observations at the AWIPEV Research Station are openly accessible via the PANGAEA data portal at Maturilli (2020), Maturilli and Dünschede (2023), respectively. In-situ precipitation and cloud datasets from the Himadri Research Station are available from the corresponding author (SD) on request.

References

Allabakash, S., Lim, S., Jang, B.-J., 2019. Melting layer detection and characterization based on range height indicator–quasi vertical profiles. Remote. Sens. 11 (23), http://dx.doi.org/10.3390/rs11232848.

Athulya, R., Nuncio, M., Chatterjee, S., Vidya, P., 2023. Characteristics of mean and extreme precipitation in ny ålesund, arctic. Atmos. Res. 295, 106989.

Atlas, D., Srivastava, R., Sekhon, R.S., 1973. Doppler radar characteristics of precipitation at vertical incidence. Rev. Geophys. 11 (1), 1–35. http://dx.doi.org/10.1029/RG011i001p00001.

Battaglia, A., Rustemeier, E., Tokay, A., Blahak, U., Simmer, C., 2010. PARSIVEL snow observations: A critical assessment. J. Atmos. Ocean. Technol. 27 (2), 333–344.

Beard, K.V., Ochs III, H.T., 1993. Warm-rain initiation: An overview of microphysical mechanisms. J. Appl. Meteorol. Clim. 32 (4), 608–625.

Bengtsson, L., Hodges, K.I., Koumoutsaris, S., Zahn, M., Keenlyside, N., 2011. The changing atmospheric water cycle in polar regions in a warmer climate. Tellus A: Dyn. Meteorol. Ocean. http://dx.doi.org/10.1111/j.1600-0870.2011.00534.x.

Bintanja, R., Selten, F., 2014. Future increases in arctic precipitation linked to local evaporation and sea-ice retreat. Nature 509 (7501), 479–482. http://dx.doi.org/10.1038/nature13259.

Bintanja, R., van der Wiel, K., van der Linden, E.C., Reusen, J., Bogerd, L., Krikken, F., Selten, F.M., 2020. Strong future increases in arctic precipitation variability linked to poleward moisture transport. Sci. Adv. 6 (7), eaax6869. http://dx.doi.org/10.1126/sciadv.aax6869.

Böhm, H.P., 1989. A general equation for the terminal fall speed of solid hydrometeors. J. Atmos. Sci. 46 (15), 2419–2427.

Boudala, F.S., Lachapelle, M., Isaac, G.A., Milbrandt, J.A., Michelson, D., Reed, R., Holden, S., 2025. Observations of the microphysics and type of wintertime mixed-phase precipitation, and instrument comparisons at sorel, quebec, Canada. Remote. Sens. 17 (6), http://dx.doi.org/10.3390/rs17060945.

Bringi, V.N., Chandrasekar, V., 2001. Polarimetric Doppler Weather Radar: Principles and Applications. Cambridge University Press.

Casella, D., Panegrossi, G., Sanò, P., Marra, A.C., Dietrich, S., Johnson, B.T., Kulie, M.S., 2017. Evaluation of the GPM-dpr snowfall detection capability: Comparison with CloudSat-CPR. Atmos. Res. 197, 64–75. http://dx.doi.org/10.1016/j.atmosres.2017.06.018.

Das, S., Maitra, A., 2016. Vertical profile of rain: Ka band radar observations at tropical locations. J. Hydrol. 534, 31–41. http://dx.doi.org/10.1016/j.jhydrol.2015.12.053.

Das, S., Shukla, A.K., Maitra, A., 2010. Investigation of vertical profile of rain microstructure at ahmedabad in Indian tropical region. Adv. Space Res. 45 (10), 1235–1243. http://dx.doi.org/10.1016/j.asr.2010.01.001.

Dorff, H., Konow, H., Schemann, V., Ament, F., 2024. Observability of moisture transport divergence in arctic atmospheric rivers by dropsondes. Atmospheric Chem. Phys. 24 (15), 8771–8795. http://dx.doi.org/10.5194/acp-24-8771-2024.

Doviak, R.J., Zrnic, D.S., 2014. Doppler radar & weather observations. Academic Press.

Durán Alárcon, C., 2019. Ground-based remote sensing of Antarctic and Alpine solid precipitation (Ph.D. thesis). (2019GREAU024), Université Grenoble Alpes.

Ernakovich, J.G., Hopping, K.A., Berdanier, A.B., Simpson, R.T., Kachergis, E.J., Steltzer, H., Wallenstein, M.D., 2014. Predicted responses of arctic and alpine ecosystems to altered seasonality under climate change. Global Change Biol. 20 (10), 3256–3269.

Fabry, F., Zawadzki, I., 1995. Long-term radar observations of the melting layer of precipitation and their interpretation. J. Atmos. Sci. 52 (7), 838–851.

Field, P.R., Heymsfield, A.J., 2003. Aggregation and scaling of ice crystal size distributions. J. Atmos. Sci. 60 (3), 544–560.

Fitch, K.E., Hang, C., Talaei, A., Garrett, T.J., 2021. Arctic observations and numerical simulations of surface wind effects on multi-angle snowflake camera measurements. Atmos. Meas. Tech. 14 (2), 1127–1142.

Garrett, T., Fallgatter, C., Shkurko, K., Howlett, D., 2012. Fallspeed measurement and high-resolution multi-angle photography of hydrometeors in freefall. Atmos. Meas. Tech. Discuss. 5 (4), 4827–4850.

Gevorgyan, A., Ackermann, L., Huang, Y., Siems, S., Manton, M., 2022. Simulation of heavy precipitation and the production of graupel related to the passage of a cold front over the Australian snowy mountains. Mon. Weather Rev. 150 (12), 3229–3249.

GmbH, O.H., 2025. OTT parsivel-2 disdrometer manual. URL https://psl.noaa.gov/data/obs/instruments/OpticalDisdrometer.pdf.

Grazioli, J., Genthon, C., Boudevillain, B., Duran-Alarcon, C., Del Guasta, M., Madeleine, J.-B., Berne, A., 2017. Measurements of precipitation in dumont d'urville, adélie land, east antarctica. Cryosphere 11 (4), 1797–1811. http://dx.doi.org/10.5194/tc-11-1797-2017.

Gupta, A.K., Deshmukh, A., Waman, D., Patade, S., Jadav, A., Phillips, V.J., Bansemer, A., Martins, J.A., Gonçalves, F.T., 2023. The microphysics of the warm-rain and ice crystal processes of precipitation in simulated continental convective storms. Commun. Earth Environ. 4 (1), http://dx.doi.org/10.1038/s43247-023-00884-5.

Hara, Y., Suzuki, K., Kawano, T., 2024. Quantitative evaluation of graupel shape observed by new particle imaging radiosonde, rainscope – a case study of a convective cloud on 25 june 2022. SOLA 20, http://dx.doi.org/10.2151/sola.2024-025.

Hassol, S., 2004. Impacts of a Warming Arctic-Arctic Climate Impact Assessment. Cambridge University Press, http://dx.doi.org/10.1175/2010JAS3379.1.

Heymsfield, A.J., Westbrook, C., 2010. Advances in the estimation of ice particle fall speeds using laboratory and field measurements. J. Atmos. Sci. 67 (8), 2469–2482.

Houze, R.A., 2012. Orographic effects on precipitating clouds. Rev. Geophys. 50, RG1001. http://dx.doi.org/10.1029/2011RG000365.

Huige, D., Yuan, Y., Wang, Y., Yan, Q., Hua, D., 2024. Drizzle microphysical property and vertical air motions retrieval using Doppler lidar and radar measurements. Opt. Express 32, 29001–29013. http://dx.doi.org/10.1364/OE.522964.

Intrieri, J.M., Shupe, M.D., Uttal, T., McCarty, B.J., 2002. An annual cycle of arctic cloud characteristics observed by radar and lidar at SHEBA. J. Geophys. Res.: Ocean. 107 (C10), SHE 5–1–SHE 5–15. http://dx.doi.org/10.1029/2000JC000423.

Jakobson, E., Vihma, T., 2010. Atmospheric moisture budget in the arctic based on the ERA-40 reanalysis. Int. J. Climatol. 30 (14), 2175–2194. http://dx.doi.org/10.1002/joc.2039.

Jarraud, M., 2008. Guide to Meteorological Instruments and Methods of Observation (WMO-No. 8). World Meteorological Organisation, Geneva.

Kug, J., Choi, D., Jin, F., Kwon, W., Ren, H., 2010. Role of synoptic eddy feedback on polar climate responses to the anthropogenic forcing. Geophys. Res. Lett. 37 (14), http://dx.doi.org/10.1029/2010GL043673.

Liebe, H.J., Hufford, G.A., Manabe, T., 1991. A model for the complex permittivity of water at frequencies below 1 THz. Int. J. Infrared Millim. Waves 12 (7), 659–675.

Liu, P., Li, C., Wang, Y., Fu, Y., 2013. Climatic characteristics of convective and stratiform precipitation over the tropical and subtropical areas as derived from TRMM PR. Sci. China Earth Sci. 56, 375–385.

Locatelli, J.D., Hobbs, P.V., 1974. Fall speeds and masses of solid precipitation particles. J. Geophys. Res. 79 (15), 2185–2197.

Löffler-Mang, M., Joss, J., 2000. An optical disdrometer for measuring size and velocity of hydrometeors. J. Atmos. Ocean. Technol. 17 (2), 130–139.

Maahn, M., Burgard, C., Crewell, S., Gorodetskaya, I.V., Kneifel, S., Lhermitte, S., Van Tricht, K., van Lipzig, N.P., 2014. How does the spaceborne radar blind zone affect derived surface snowfall statistics in polar regions? J. Geophys. Res.: Atmos. 119 (24), 13–604. http://dx.doi.org/10.1002/2014JD022079.

Maahn, M., Kollias, P., 2012. Improved micro rain radar snow measurements using Doppler spectra post-processing. Atmospheric Meas. Tech. 5 (11), 2661–2673.

Macdonald, R.W., Harner, T., Fyfe, J., 2005. Recent climate change in the arctic and its impact on contaminant pathways and interpretation of temporal trend data. Sci. Total Environ. 342 (1–3), 5–86. http://dx.doi.org/10.1016/j.scitotenv.2004.12.059.

Maturilli, M., 2020. Continuous Meteorological Observations at Station Ny-Ålesund (2011-08 et seq). PANGAEA, Alfred Wegener Institute - Research Unit Potsdam, http://dx.doi.org/10.1594/PANGAEA.914979, URL https://doi.org/10.1594/PANGAEA.914979.

Maturilli, M., Dünschede, E., 2023. Homogenized Radiosonde Record at Station Ny-ÅLesund, Spitsbergen, 2017–2022. PANGAEA, http://dx.doi.org/10.1594/PANGAEA.961203.

Maturilli, M., Ebell, K., 2018. Twenty-five years of cloud base height measurements by ceilometer in ny-ålesund, svalbard. Earth Syst. Sci. Data 10 (3), 1451–1456. http://dx.doi.org/10.5194/essd-10-1451-2018.

Maturilli, M., Kayser, M., 2017. Arctic warming, moisture increase and circulation changes observed in the ny-ålesund homogenized radiosonde record. Theor. Appl. Climatol. 130, 1–17. http://dx.doi.org/10.1007/s00704-016-1864-0.

Mitchell, D.L., Heymsfield, A.J., 2005. Refinements in the treatment of ice particle terminal velocities, highlighting aggregates. J. Atmos. Sci. 62 (5), 1637–1644.

Nuncio, M., Athulya, R., Nandanan, N., Chatterjee, S., Satheesan, K., Acharya, A., Subeesh, M., Vidya, P., 2023. Hails in ny alesund, svalbard-atmospheric vertical structure and dependence on circulation. Nat. Hazards 117 (2), 1365–1380. http://dx.doi.org/10.1007/s11069-023-05907-0.

Nuncio, M., Satheesan, K., Acharya, A., Chatterjee, S., Subeesh, M., Athulya, R., 2022. A southerly wind event and precipitation in ny ålesund, arctic. J. Atmos. Sol.-Terr. Phys. 231, 105869. http://dx.doi.org/10.1016/j.jastp.2022.105869.

Oue, M., Kumjian, M.R., Lu, Y., Jiang, Z., Clothiaux, E.E., Verlinde, J., Aydin, K., 2015. X-Band polarimetric and ka-band Doppler spectral radar observations of a graupel-producing arctic mixed-phase cloud. J. Appl. Meteorol. Clim. 54 (6), 1335–1351. http://dx.doi.org/10.1175/JAMC-D-14-0315.1.

Oyj, V., 2022. Ceilometer CL51 datasheet (b210861en-g.1). Retrieved June 6, 2024. https://docs.vaisala.com/v/u/B210861EN-G.1/en-US.

Palerme, C., Kay, J., Genthon, C., l'Ecuyer, T., Wood, N., Claud, C., 2014. How much snow falls on the antarctic ice sheet? Cryosphere 8 (4), 1577–1587. http://dx.doi.org/10.5194/tc-8-1577-2014.

Peters, G., Fischer, B., Andersson, T., 2002. Rain observations with a vertically looking micro rain radar (MRR). Boreal Environ. Res. 7 (4), 353–362.

Pruppacher, H.R., Klett, J.D., Wang, P.K., 1998. Microphysics of Clouds and Precipitation. Taylor & Francis.

Przybylak, R., Sadourny, R., Mysak, L.A., 2003. The climate of the Arctic. Springer.

Rangno, A., 2015. CLOUDS AND FOG | classification of clouds. In: North, G.R., Pyle, J., Zhang, F. (Eds.), Encyclopedia of Atmospheric Sciences (Second Edition), second ed. Academic Press, Oxford, pp. 141–160. http://dx.doi.org/10.1016/B978-0-12-382225-3.00112-2.

Saini, L., Das, S., Murukesh, N., 2025. Case studies of different types of precipitation at ny-ålesund, arctic. Sci. Rep. 15 (1), 3086.

Sarkar, T., Das, S., Maitra, A., 2015. Assessment of different raindrop size measuring techniques: Inter-comparison of Doppler radar, impact and optical disdrometer. Atmos. Res. 160, 15–27. http://dx.doi.org/10.1016/j.atmosres.2015.03.001.

Schumacher, C., Houze Jr., R.A., 2006. Stratiform precipitation production over sub-saharan africa and the tropical east atlantic as observed by TRMM. Q. J. R. Meteorol. Soc.: A J. of Atmospheric Sci. Appl. Meteorol. Phys. Ocean. 132 (620), 2235–2255. http://dx.doi.org/10.1256/qj.05.121.

Serreze, M.C., Barrett, A.P., Slater, A.G., Steele, M., Zhang, J., Trenberth, K.E., 2007. The large-scale energy budget of the arctic. J. Geophys. Res.: Atmos. 112 (D11).

Serreze, M.C., Barrett, A., Stroeve, J., Kindig, D., Holland, M., 2009. The emergence of surface-based arctic amplification. Cryosphere 3 (1), 11–19.

Shupe, M.D., Uttal, T., Matrosov, S.Y., 2005. Arctic cloud microphysics retrievals from surface-based remote sensors at SHEBA. J. Appl. Meteorol. 44 (10), 1544–1562.

Society, A.M., 2025. Rain and snow mixed — Glossary of Meteorology. https://glossary.ametsoc.org/wiki/Rain_and_snow_mixed. (Accessed 16 August 2025).

Solomon, S., Qin, D., Manning, M., Averyt, K., Marquis, M., 2007. Climate change 2007-the physical science basis: Working group I contribution to the fourth assessment report of the IPCC, vol. 4, Cambridge University Press.

Suh, S.-H., Kim, H.-I., Choi, E.-H., You, C.-H., 2021. Estimation of liquid fraction of wet snow by using 2-D video disdrometer and S-band weather radar. Remote. Sens. 13 (10), http://dx.doi.org/10.3390/rs13101901.

Tokay, A., Wolff, D.B., Petersen, W.A., 2014. Evaluation of the new version of the laser-optical disdrometer, ott parsivel 2. J. Atmos. Ocean. Technol. 31 (6), 1276–1288.

Wallace, J.M., Hobbs, P.V., 2006. Atmospheric science: an introductory survey, vol. 92, Elsevier.

Walsh, J.E., Chapman, W.L., 1998. Arctic cloud–radiation–temperature associations in observational data and atmospheric reanalyses. J. Clim. 11 (11), 3030–3045. http://dx.doi.org/10.1175/1520-0442(1998)011<3030:ACRTAI>2.0.CO;2.

Wolfensberger, D., Scipion, D., Berne, A., 2016. Detection and characterization of the melting layer based on polarimetric radar scans. Q. J. R. Meteorol. Soc. 142 (S1), 108–124. http://dx.doi.org/10.1002/qj.2672.

Wood, R., 2005. Drizzle in stratiform boundary layer clouds. Part I: Vertical and horizontal structure. J. Atmos. Sci. 62 (9), 3011–3033. http://dx.doi.org/10.1175/JAS3529.1.

Zhou, L., Zhou, Y., Fu, Z., Lü, J., Lu, C., Xiao, H., 2024. Vertical structures and microphysical mechanisms of winter precipitation over the southwestern mountainous area of China. Atmos. Res. 303, 107346. http://dx.doi.org/10.1016/j.atmosres.2024.107346.